

An *XMM-Newton* Study of Six Narrow-Line Seyfert 1 Galaxies at $z = 0.35 - 0.92$

Zhibo Yu,^{1,2,3*} Jiachen Jiang,⁴ Cosimo Bambi,³ Luigi C. Gallo,⁵ Dirk Grupe,⁶ Andrew C. Fabian,⁴ Christopher S. Reynolds,⁴ William N. Brandt^{1,2,7}

¹*Department of Astronomy and Astrophysics, The Pennsylvania State University, 525 Davey Lab, University Park, PA 16802, USA*

²*Institute for Gravitation and the Cosmos, The Pennsylvania State University, University Park, PA 16802, USA*

³*Center for Field Theory and Particle Physics and Department of Physics, Fudan University, 2005 Songhu Road, Shanghai 200438, China*

⁴*Institute of Astronomy, University of Cambridge, Madingley Road, Cambridge CB3 0HA, UK*

⁵*Department of Astronomy and Physics, Saint Mary's University, 923 Robie Street, Halifax, NS, B3H 3C3, Canada*

⁶*Department of Physics, Geology, and Engineering Technology, Northern Kentucky University, Nunn Drive, Highland Heights, KY 41099, USA*

⁷*Department of Physics, The Pennsylvania State University, 104 Davey Laboratory, University Park, PA 16802, USA*

Accepted XXX. Received YYY; in original form ZZZ

ABSTRACT

We report a detailed analysis of the *XMM-Newton* spectra of six Narrow-Line Seyfert 1 (NLS1) galaxies at redshift $z = 0.35-0.92$. Compared with the NLS1s at lower redshift in the previously most-studied sample, these NLS1s have larger black hole (BH) masses ($\log M_{\text{BH}} > 7.5$) with similar or even lower Eddington ratios. Our extended *XMM-Newton* sample of NLS1s shows strong soft X-ray excess emission below 2 keV. The quantified soft excess strength does not show an obvious discrepancy from previous studies of the lower-redshift NLS1s. The systematic effect in the measurement of the Eddington ratio mainly lies in the bolometric correction factor. We also tentatively fit the spectra assuming two more physical models for the soft excess: warm Comptonization and relativistic reflection from the inner accretion disk. In the first scenario, we confirm the ubiquity of a warm and optically thick corona. The behavior of a single source can be better explained by relativistic reflection, although we cannot distinguish which model is a more favorable explanation for the soft excess based on the best-fit statistics.

Key words: accretion, accretion discs – black hole physics – galaxies: Seyfert – X-rays: galaxies

1 INTRODUCTION

1.1 Seyfert 1 galaxies and NLS1s

Active Galactic Nuclei (AGNs) radiate across the electromagnetic spectrum from radio to γ -ray, often even brighter than the rest of their host galaxies (Frank et al. 2002). Seyfert galaxies are one class of active galaxies with luminous nuclei (Peterson 1997). Depending upon the width of the emission lines in the spectrum, Seyfert galaxies are classified into Seyfert 1 and 2 galaxies. Seyfert 1 galaxies are characterized by broad (corresponding to a velocity of $\approx 10^4$ km s⁻¹) permitted lines and narrow forbidden lines, while the permitted lines in Seyfert 2 galaxies are similar but narrower ($\lesssim 10^3$ km s⁻¹) (Karttunen et al. 2007). Narrow-line Seyfert 1 (NLS1) galaxies are a subclass of Seyfert 1 introduced in Osterbrock & Pogge (1985). They show similar spectral properties, but the line widths are small compared with their broad-line counterparts. NLS1s are defined by a narrow permitted H β line with full width at half maximum (FWHM) < 2000 km s⁻¹, [O III]/H β < 3 (Osterbrock & Dahari 1983; Goodrich 1989) and often strong Fe II emission.

NLS1s are believed to host relatively lower-mass supermassive black holes (BHs) with $M_{\text{BH}} < 10^8 M_{\odot}$ and have high luminosities $L \gtrsim 0.1 L_{\text{Edd}}$ compared with BLS1s (e.g. Boller et al. 1996;

Grupe & Mathur 2004; Yuan et al. 2007; Rakshit et al. 2017; Waddell & Gallo 2020), where $L_{\text{Edd}} = 1.26 \times 10^{38} (M_{\text{BH}}/M_{\odot}) \text{ erg s}^{-1}$ is the Eddington luminosity. L/L_{Edd} is likely to be interpreted as the eigenvector 1, a basic parameter that describes the relationship between the properties such as the X-ray spectral index α_{X} , the Fe II strength, and FWHM(H β) (Boroson & Green 1992; Boroson 2002; Grupe 2004), and is sometimes interpreted as the “age” of the AGN (Grupe et al. 1999). In this context, NLS1s can be regarded as AGNs with a high L/L_{Edd} in the early phase of their evolution.

1.2 X-ray View of NLS1s and Soft X-ray Excess

The temperature of the accretion disk in an AGN is $\sim 10^5$ K, which results in blackbody emission that peaks in the far ultraviolet (UV) band. However, due to strong Galactic extinction, a majority of the spectral energy distribution (SED) in this band cannot be observed. In the innermost region, a compact, hot ($kT \sim 100$ keV), and optically thin corona is responsible for the hard X-ray power-law continuum due to inverse Comptonization of the disk photons (Haardt & Maraschi 1991; Fabian et al. 2015). The Comptonized photons also illuminate the disk where they are reprocessed within a Thompson optical depth and produce a reflection spectrum. This component includes a series of emission lines and a Compton hump peaking at 20 – 40 keV. The most prominent feature in the reflection spectrum

* E-mail: zvy5225@psu.edu

is the iron $K\alpha$ emission line around 6.4 keV (Ross & Fabian 1993; Fabian et al. 2002; Reynolds & Nowak 2003; Jiang et al. 2018a).

NLS1s show unique properties in X-ray bands such as steep soft X-ray spectra at 0.2 – 2 keV and extreme X-ray variability (Boller et al. 1996; Leighly 1999; Grupe et al. 2001; Gallo 2018). Gallo (2006) defined two samples of NLS1s, the “complex” sample, which shows significant spectral complexity and weaker X-ray luminosity at 2.5 – 10 keV, and the “simple” sample that does not strongly deviate from a power-law continuum. The “complex” samples can+ either be explained by a partial-covering absorption model that obscures the X-ray emitting region (Tanaka et al. 2004), or a light-bending model in the disk-reflection scenario (Miniutti & Fabian 2004).

The soft X-ray excess is a common phenomenon in many NLS1s and remains an active research topic. It refers to the excess of X-rays below 2 keV with respect to the extrapolation of the hard X-ray continuum. Studies of AGN samples have demonstrated that the soft excess is ubiquitous in both NLS1s and BLS1s, with stronger soft excess strength in NLS1s (e.g. Middleton et al. 2007a; Bianchi et al. 2009; Gliozzi & Williams 2020).

There are now two popular competing models that are able to account for the soft excess. One is the warm Comptonization model. It assumes a warm ($kT_e \sim 0.5\text{--}1$ keV) and optically thick ($\tau \sim 5\text{--}10$) corona in addition to the hot corona. The Comptonization of the disk UV photons in the warm corona is responsible for the soft excess (e.g. Jin et al. 2009, 2012; Petrucci et al. 2018). An alternative model is the relativistic blurred disk-reflection model. The emission lines in the soft X-ray band from the reflection component are blurred due to relativistic effects near the black hole and thus constitute the soft excess (e.g. Crummy et al. 2006; Jiang et al. 2020). The reflection model is also supported by the evidence of soft X-ray reverberation lags (Fabian et al. 2009; Alston et al. 2020).

In addition to explaining the soft excess, the relativistic reflection models can also provide a window to understand the innermost geometry of NLS1s and the physics of accretion (Bambi et al. 2021; Reynolds 2021). Black hole spin (a_*) measurement is an active topic, and it is still an ongoing effort. One of the most credible and robust techniques for measuring the black hole spin is to model the relativistic reflection features. The reflection spectrum will be distorted and broadened by relativistic effects of Doppler broadening from the fast orbital motion, the gravitational redshift, and the light-bending due to the black hole’s strong gravitational field (Fabian et al. 1989; Miller et al. 2002; Miller 2007). There are various spin measurements of the supermassive black holes in AGNs, e.g. MCG–6–30–15 ($a_* = 0.91^{+0.06}_{-0.07}$; Marinucci et al. 2014), Mrk 335 ($a_* = 0.83^{+0.10}_{-0.13}$; Parker et al. 2014), IRAS 13224–3809 ($a_* > 0.99$; Jiang et al. 2018b), H1821+643 ($a_* = 0.62^{+0.22}_{-0.37}$; Sisk-Reynés et al. 2022) using the X-ray reflection technique. Despite that these measurements inevitably suffer from several systematic effects (Laor 2019), the relativistic reflection is a robust signature. Apart from spin measurement, it is capable of probing the physical properties in the innermost region where strong relativistic effects dominate. As we observe the hard X-ray component produced by the hot compact corona, we can estimate the properties and the geometry of the corona (e.g. Markoff et al. 2005; Wilkins & Fabian 2012; Parker et al. 2018).

Apart from testing different physical models, an alternative approach to study the soft excess would be to quantitatively identify the soft excess strength regardless of the spectral components (e.g. Picconcelli et al. 2005; Boissay et al. 2016). Gliozzi & Williams (2020) (hereafter GW+20) conducted a model-independent correlation analysis of a clean sample of 68 objects (46 BLS1s and 22 NLS1s) in which they quantified the soft excess strength. However, this study only included NLS1s in the local universe (median $z = 0.08$, with

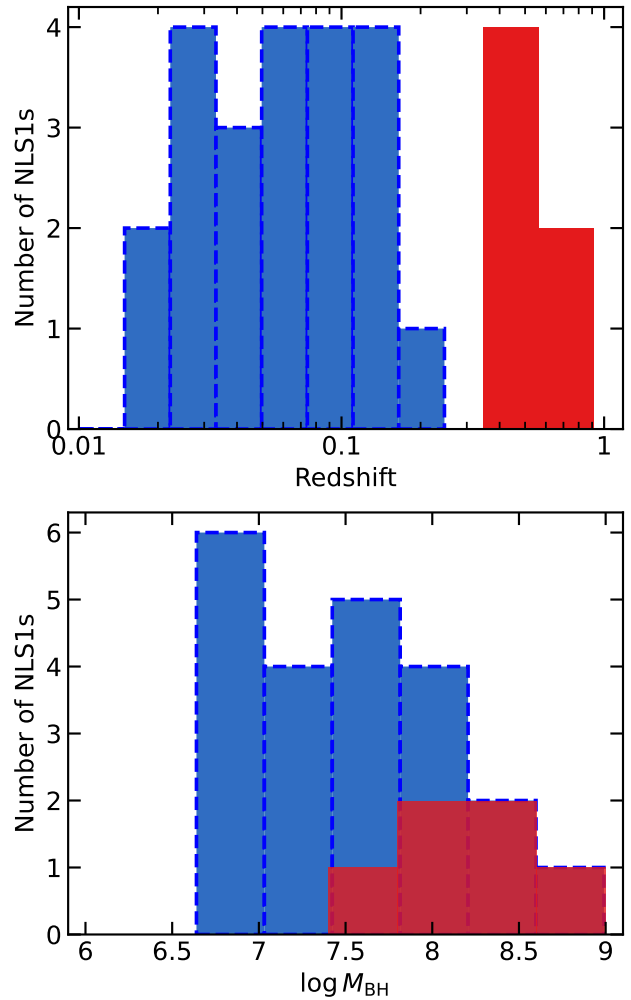


Figure 1. The distribution of the redshifts and the BH masses in our sample (in red). The NLS1s at lower redshifts in GW+20 are shown in blue with dashed edges.

one outlier at $z = 0.24$) using the 0.5 – 10 keV spectra. We want to extend the study to higher redshifts.

In this study, we collect six NLS1s at redshift $0.35 < z < 0.92$ with sufficient count rates from the literature. We want to first examine whether these NLS1s at higher redshift have prominent soft excess emission. If they do, then we will further quantify the soft excess strength and compare the results with the ones in GW+20. In particular, the NLS1s at higher redshift in our sample have relatively higher black hole masses than the NLS1 sample in GW+20. It is, therefore, interesting to compare the strength of the soft excess emission in these two samples. Although our NLS1s’ observations do not have high enough signal-to-noise ratios (SNRs) to distinguish different soft excess modes as in previous work (e.g., Middleton et al. 2007b; Boissay et al. 2016; Jiang et al. 2018b; García et al. 2019), we tentatively test for the warm corona and relativistic reflection models and find whether the two models provide consistent explanations to the soft excess emission of our sample as before, e.g., similar warm corona temperatures or similar disk densities.

The paper is structured as follows. Section 2 describes our sample and data reduction. In Section 3, we present our analysis and

Table 1. List of NLS1s analyzed in this work.

Source	Full Name	<i>z</i>	$\log M_{\text{BH}}/M_{\odot}$	XMM-Newton ObsID	Date	Net Exposure ^e ks	Galactic N_{H} $\times 10^{20} \text{ cm}^{-2}$
E1346+266	E1346+266	0.92	8.63 ± 0.13^a	0109070201	2003-01-13	48, 55, 55	1.25
PG 1543+489	PG 1543+489	0.40	8.13 ± 0.33^b	0153220401	2003-02-08	9, 12, 12	1.67
				0505050201	2007-06-09	11, 16, 17	
				0505050701	2007-06-15	13, 16, 16	
SDSS J020435	SDSS J020435.18–093154.9	0.62	8.20 ± 0.31^c	0763910301	2015-08-08	–, 11, 12	2.42
SDSS J024651	SDSS J024651.91–005930.9	0.47	8.29 ± 0.15^c	0402320101	2007-02-02	8, 11, 11	4.27
WISEA J033429	WISEA J033429.44+000610.9	0.35	7.83 ± 0.13^d	0402320201	2007-02-02	8, 10, 10	9.85
1WGA J2223	1WGA J2223.7–0206	0.46	7.55 ± 0.14^d	0090050601	2001-12-06	15, –, –	5.70

Notes: The BH masses are measured based on the line width of ^a Mg II Shen et al. (2011); ^b H β Kelly et al. (2008); ^c Mg II Wang et al. (2009). Based on ^d RM method with H β , Kaspi et al. (2000); Grandi et al. (2004). ^e The net exposure is reported in the order of EPIC-pn, EPIC-MOS1, and EPIC-MOS2. SDSS J020435 lacks pn data; 1WGA J2223 lacks MOS1 and MOS2 data.

discussions. Specifically, in the first two subsections, we introduce our baseline models and illustrate the soft excess in our sample. In Section 3.3, we quantify the soft excess and compare the results with the lower-redshift sample in GW+20. In Section 4.1, we discuss the systematic uncertainties and the selection effects in our analysis. In Section 4, we apply the two possible physical models for the soft excess: the warm Comptonization model and the relativistic reflection model to see whether we can have further physical interpretations. Finally, in Section 5 we draw our conclusions and point out prospects.

2 OBSERVATION SAMPLE AND DATA REDUCTION

We select six NLS1s with redshift $0.35 < z < 0.92$ observed by the European Space Agency’s XMM-Newton satellite (Jansen et al. 2001). Details about the observations are summarized in Table 1. Their redshift and BH mass distributions are shown in Figure 1. The studied redshift range is extended much beyond the one in the previous sample. The BH masses are distributed at the upper end of the previous sample, which are estimated by the Reverberation Mapping (RM) method or the emission-line properties (see the notes in the Table for details). In addition, we include the FWHM(H β) and Fe II/H β ratios from the literature in Table 2. We also show the full list of our candidate samples with their EPIC-pn count rates in Appendix A. We do not aim to conduct a thorough study of the entire population of NLS1s at the given redshift range. Instead, we want to examine how these selected NLS1s behave given their higher redshift and the M_{BH} at the upper end of the local sample. Future systematic studies of the NLS1s at higher redshift can be carried out with archived XMM-Newton data of NLS1 in catalogs (e.g., Rakshit & Stalin 2017)

We use the European Photon Imaging Camera (EPIC) observations collected by EPIC-pn and EPIC-MOS (Strüder et al. 2001; Turner et al. 2001). Note that SDSS J020435 only has available EPIC-MOS data; 1WGA J2223 only has available EPIC-pn data. Both sources fall into the gaps of the CCD chips in the FoV of either EPIC-pn or EPIC-MOS. We use the XMM-Newton Science Analysis System (SAS) v20.0.0 software package to reduce the data. We first generate the clean event files using epproc (emproc) for EPIC-pn observations (EPIC-MOS observations). We then extract the good time intervals (GTIs) by selecting the time intervals with weak flaring particle backgrounds. For PG 1543+489, due to strong background flaring in all observations, we apply the iterative 3σ cleaning procedure for the EPIC 10 – 15 keV range described in Vignali et al. (2008). For other observations, we use the standard EPIC data reduction thread, where we select the single event (PATTERN=0) count rate in the ≥ 10 keV

band that is smaller than $0.40 \text{ counts s}^{-1}$ ($0.35 \text{ counts s}^{-1}$) for EPIC-pn (EPIC-MOS) data. Then we filter the event lists for all observations by selecting single and double events for EPIC-pn (PATTERN ≤ 4) and EPIC-MOS (PATTERN ≤ 12) in a circular region. No pile-up issue is found in our observations. The backgrounds are extracted in nearby regions on the same chip. The redistribution matrix files and ancillary response files are generated by rmfgen and arfgen.

We use EPIC spectra in the 0.3 – 10 keV energy range in our analysis. Given the redshift range of our sample, the analyzed rest-frame energy band is consistent with the GW+20 local samples which were analyzed in the 0.5 – 10 keV band. The lightcurves of our samples do not show strong X-ray variability. For PG 1543+489, we use the epicspeccombine tool to stack the three observations from EPIC-pn, EPIC-MOS1, and EPIC-MOS2 spectra, respectively. We group the spectra using the specgroup command so that each bin has a minimum signal-to-noise ratio (SNR) of 3 (minimum SNR of 6 for PG 1543+489) and a minimum width of 1/3 of the full width half maximum resolution at the central energy of the group.

3 SPECTRAL ANALYSIS

We use Xspec v12.12.0 (Arnaud 1996) and the χ^2 statistics in our analysis. The Galactic hydrogen column density N_{H} is calculated according to Willingale et al. (2013), which is shown in Table 1. The luminosity distance d_{L} is retrieved from the NED website¹, where $H_0 = 67.8 \text{ km s}^{-1} \text{ Mpc}^{-1}$, $\Omega_{\text{matter}} = 0.308$, and $\Omega_{\text{vacuum}} = 0.692$ are assumed.

3.1 Soft Excess Emission

We fit the 2 – 10 keV energy band in the observed frame with an absorbed powerlaw at the Galactic column density values (0.7 – 10 keV for SDSS J020435 and WISEA J033429 due to inadequate data bins in the 2 – 10 keV band). We then include the 0.3 – 2 keV band data without re-fitting to illustrate the soft excess emission in our sources. We show the data/model ratio plots in Figure 2. All spectra show strong excess emission in the soft X-ray band below 1 keV. To model the soft excess component, we continue to apply a baseline model to the spectra.

¹ <https://ned.ipac.caltech.edu/>

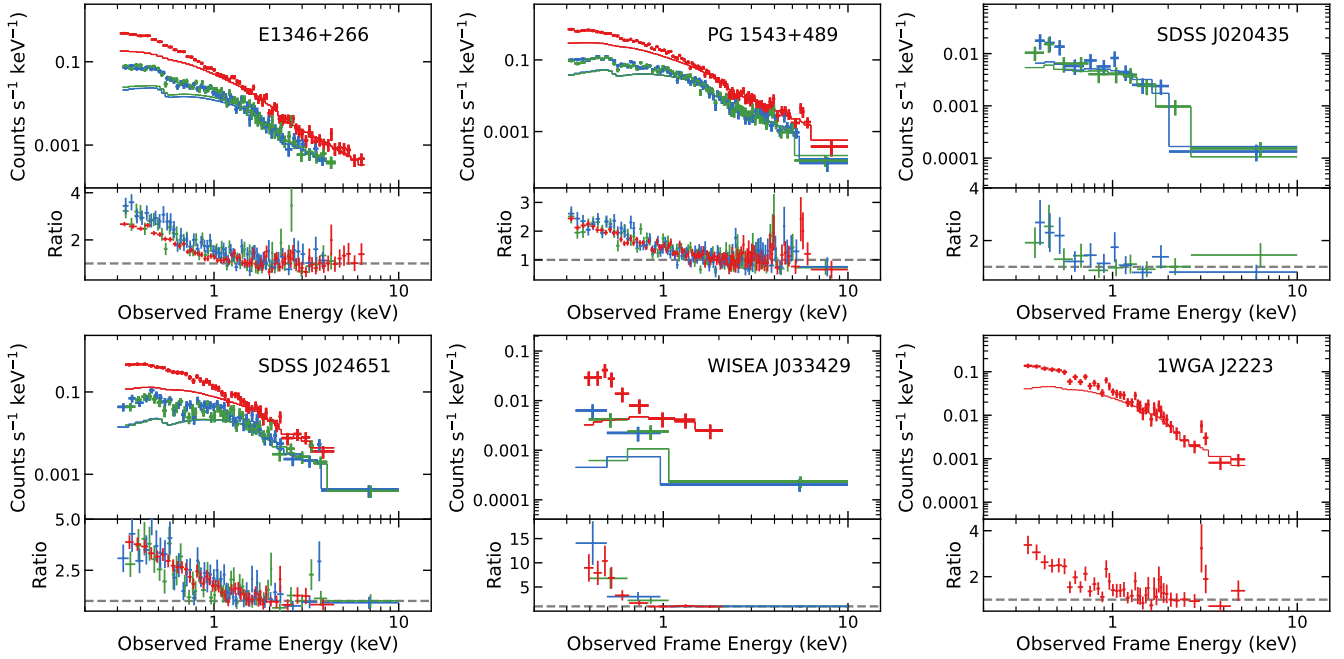


Figure 2. Count spectra and data-to-model ratio plots showing the soft excess of the NLS1s in this work. The upper plots show the count spectra and the corresponding absorbed powerlaw models. The lower plots show the data-to-model ratio. The red, blue, and green data (lines) correspond to pn, MOS1, and MOS2 data (models).

3.2 Baseline Models and Eddington Ratio

We apply a phenomenological baseline model across the available energy band of 0.3 – 10 keV in the observed frame. Our baseline model is

$$\text{const} \times \text{TBabs} \times \text{zshift} \times (\text{bbody} + \text{powerlaw})$$

in Xspec notation. We use `powerlaw` to model the high-energy Comptonized continuum, and we use the blackbody model `bbody` with the temperature at kT to fit the soft excess emission. The `const` is to account for the flux calibration uncertainties. The `zshift` model accounts for the redshift. The `Tbabs` model describes the absorption along the line-of-sight. As a first attempt, we allow the column density N_{H} to vary. We shall show all our spectral plots in the rest frame of the sources.

The iron $K\alpha$ emission feature around 6.4 keV is produced by the illumination of the disk by the primary X-ray source and the fluorescence of Fe K-shell electrons (Fabian et al. 1989; Miller 2007). This feature is not prominent in our sample due to the low signal-to-noise ratio (SNR) in the iron emission band. Thus, we cannot conclude the existence of the iron $K\alpha$ line in most objects. However, Vignali et al. (2008) found evidence of a broad iron $K\alpha$ emission line in PG1543+489, so we consider an additional component for the iron $K\alpha$ emission for this source in our analysis by following the same approach as in Vignali et al. (2008).

For PG 1543+489, we add a `relline` (Dauser et al. 2010) component to model the relativistic iron $K\alpha$ emission feature. We set the rest-frame emission line energy E_{line} at 6.7 keV as it is the best-fit value obtained by Vignali et al. (2008). The illumination pattern onto the disk, namely the emissivity profile $\epsilon(r)$ is assumed to be a broken-powerlaw: $\epsilon(r) \propto r^{-q_{\text{in}}}$ for $r < R_{\text{br}}$, and $\epsilon(r) \propto r^{-3}$ for $r > R_{\text{br}}$, where q_{in} is the inner emissivity index and R_{br} is the break-

ing radius. We also allow a free BH spin a_* and inclination angle θ .

Figure 3 shows the best-fit models and data/model ratio plots for the six sources. Table 3 gives the best-fit results using the baseline models. We find that the N_{H} cannot be constrained in our fits, so we fix the N_{H} to the Galactic values throughout our analysis. We also report the N_{H} upper limit within 90% confidence level in column (13) of Table 2. None of the sources are highly obscured. Based on the best fits, we measure the X-ray luminosity L_{X} from 2 – 10 keV in the rest frame after correcting for the Galactic absorption. We calculate the logarithmic Eddington ratio $\log \lambda_{\text{Edd}} = \log(L_{\text{bol}}/L_{\text{Edd}})$, where L_{bol} is the bolometric luminosity, with the BH mass given in Table 1. The bolometric correction factor k_{bol} linking the 2 – 10 keV L_{X} and the L_{bol} is estimated by the approximation in Netzer (2019):

$$k_{\text{bol}} = 7 \times (L_{\text{X}, 2-10 \text{ keV}} / 10^{42} \text{ erg s}^{-1})^{0.3}. \quad (1)$$

We also present the measurements of $\log \lambda_{\text{Edd}}$ by optical observations in the literature. The results are summarized in columns (7), (8), and (9) of Table 2 (see the notes therein for more information). All sources present large $\log \lambda_{\text{Edd}} > -1$ estimated from the X-rays except for WISEA J033429. The large Eddington ratio of our sample is consistent with the typical NLS1 behavior that they are actively accreting matter.

3.3 The Soft Excess Strength: Comparison with BLS1s and NLS1s at lower redshifts

Literature shows a number of ways to quantify the soft excess strength (e.g. Piconcelli et al. 2005; Petrucci et al. 2013; Boissay et al. 2016). Here we adapt the three quantities defined in GW+20 to characterize the soft excess strength.

$SX1$ is defined as the ratio of the unabsorbed 0.5 – 2 keV flux in

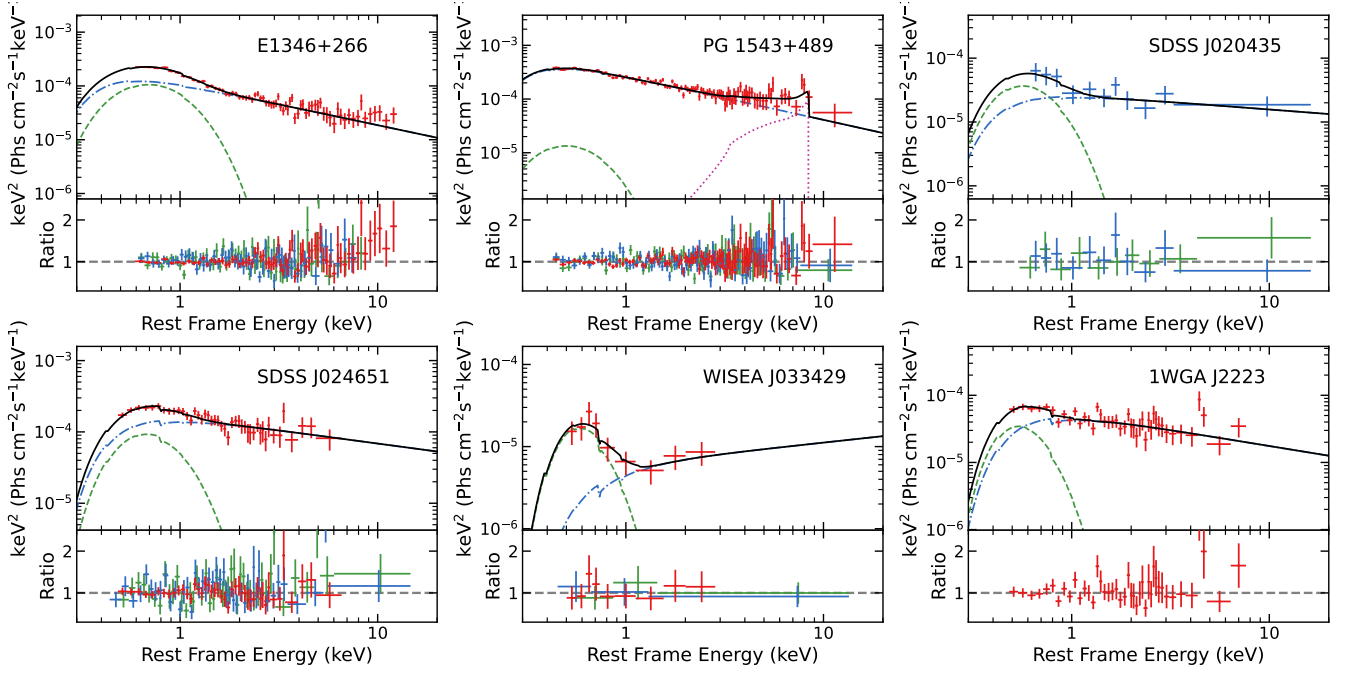


Figure 3. Baseline model fits. Unfolded best-fit model plots and data-to-model ratio plots for each NLS1. The bbody model is used to fit their soft excess emission. The upper plots show the best-fit models. We only show the pn data in red for clarity (MOS1 data in blue for SDSS J020435). Solid black lines: the total model; blue dash-dotted lines: powerlaw; green dashed lines: bbody. The lower plots show the data-to-model ratios. The red, blue, and green data points correspond to pn, MOS1, and MOS2 data.

Table 2. The optical, UV, and X-ray properties of our NLS1 sample. (1) Source Name; (2) $\text{Fe II}/\text{H}\beta$; (4) rest-frame 2500 Å flux density ($\times 10^{-27} \text{ erg s}^{-1} \text{ cm}^{-2} \text{ Hz}^{-1}$); (5) rest-frame 2 keV flux density ($\times 10^{-31} \text{ erg s}^{-1} \text{ cm}^{-2} \text{ Hz}^{-1}$); (6) α_{OX} ; (7) rest-frame 2 – 10 keV X-ray luminosity ($\times 10^{43} \text{ erg s}^{-1}$); (8) X-ray Eddington ratio measured by Equation 1; (9) Optical Eddington ratio reported in literature; (10) $SX1$; (11) $SX2$; (12) $SX3$; (13) N_{H} upper limit ($\times 10^{20} \text{ cm}^{-2}$).

(1)	(2)	(3)	(4)	(5)	(6)	(7)	(8)	(9)	(10)	(11)	(12)	(13)
Source	$\text{Fe II}/\text{H}\beta$	$\text{FWHM}(\text{H}\beta)$	f_{UV}	f_{X}	α_{OX}	L_{X}	$\log \lambda_{\text{Edd,X}}$	$\log \lambda_{\text{Edd,opt}}$	$SX1$	$SX2$	$SX3$	N_{H}
E1346+266	0.98	1840	0.30	2.16	-1.21	42.5	-0.465	-0.687 ^a	$0.62^{+0.11}_{-0.12}$	$0.44^{+0.07}_{-0.08}$	$13.5^{+1.8}_{-2.2}$	1.6
PG 1543+489	0.86	1560	10.0	5.03	-1.65	16.6	-0.495	0.369 ^b	$0.017^{+0.005}_{-0.017}$	$0.02^{+0.01}_{-0.03}$	$0.4^{+0.2}_{-0.5}$	2.9
SDSS J020435	0.83	1905	1.40	0.74	-1.64	8.5	-0.94	-0.466 ^c	$0.7^{+0.5}_{-0.7}$	$0.4^{+0.2}_{-0.3}$	4^{+2}_{-4}	29
SDSS J024651	0.49	1725	3.83	4.04	-1.53	21	-0.52	-0.356 ^c	$0.41^{+0.15}_{-0.24}$	$0.24^{+0.08}_{-0.14}$	5^{+2}_{-3}	7.9
WISEA J033429	0.69	2127	3.46	0.23	-1.99	1.4	-1.60	-0.551 ^c	$2.1^{+1.3}_{-1.9}$	$0.8^{+0.4}_{-0.5}$	$2.0^{+0.6}_{-1.0}$	91
1WGA J2223	—	2000	1.09	1.21	-1.52	8.3	-0.31	$> -0.170^d$	$0.36^{+0.14}_{-0.20}$	$0.23^{+0.08}_{-0.12}$	8^{+3}_{-4}	13

Notes: The optical Eddington ratios are collected from ^a Shen et al. (2011). ^b Baskin & Laor (2004). ^c Rakshit & Stalin (2017). ^d Grandi et al. (2004).

the rest frame of the blackbody component over the Comptonized component:

$$SX1 = \left(\frac{F_{\text{bb}}}{F_{\text{cp}}} \right)_{0.5-2 \text{ keV}}$$

Similarly, $SX2$ is the ratio of the unabsorbed rest-frame 0.5–10 keV flux of the blackbody component over the Comptonized component:

$$SX2 = \left(\frac{F_{\text{bb}}}{F_{\text{cp}}} \right)_{0.5-10 \text{ keV}}$$

Finally, $SX3$ is the ratio of the unabsorbed rest-frame 0.5 – 2 keV blackbody luminosity over the Eddington luminosity:

$$SX3 = \frac{L_{\text{bb},0.5-2 \text{ keV}}}{L_{\text{Edd}}}$$

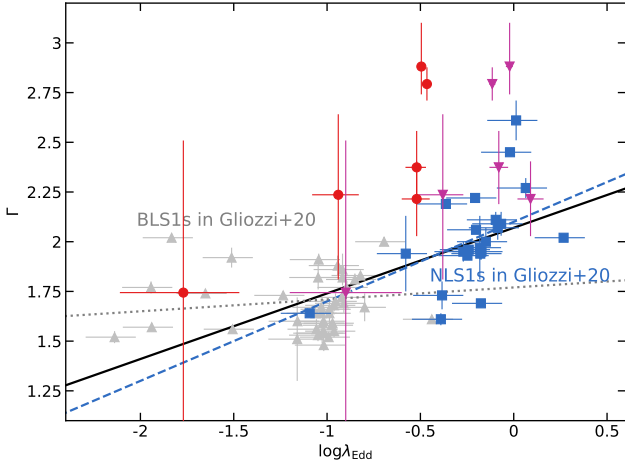
We measure $SX1$, $SX2$, and $SX3$ using the baseline models defined

in Section 3.2, where bbody is the phenomenological description of the soft excess, and the Comptonized component is modeled by powerlaw. All flux measurements are based on the model extrapolation in the rest-frame energy band. Columns (10), (11), and (12) in Table 2 summarize the measurements of the soft excess strength.

We compare the results of our sample with the NLS1s and BLS1s at lower redshift in GW+20. While their NLS1s have a median $z = 0.08$ with one outlier at $z = 0.24$, our sample spans from $z = 0.35$ to $z = 0.92$, which is beyond the previous sample's range. In Figures 4, 5, and 6, the red circles are our NLS1 sample at higher redshift; the blue squares and the grey triangles are the NLS1s and BLS1s measured in GW+20. Figure 4 shows the correlations between the photon index Γ and the $\log \lambda_{\text{Edd}}$. Our NLS1s roughly follow the positive trend between Γ and $\log \lambda_{\text{Edd}}$ as revealed by the GW+20 sample. They also show similar photon indices to the lower-redshift sources, but the λ_{Edd} is slightly lower. This comparison is band-consistent. Considering the difference in redshift, we conclude the

Table 3. Best-fit table of the baseline models. The flux F is in units $\text{erg s}^{-1} \text{cm}^{-2}$. The reported uncertainties correspond to the 90% confidence level for one parameter ($\Delta\chi^2 = 2.71$). * indicates that the parameter is frozen in the fit.

	E1346+266	PG1543+489	SDSS J0204	SDSS J0246	WISEA J033	1WGA J2223
bbody						
kT (keV)	$0.153^{+0.008}_{-0.009}$	< 0.16	$0.11^{+0.07}_{-0.06}$	$0.14^{+0.02}_{-0.02}$	$0.09^{+0.03}_{-0.03}$	$0.08^{+0.03}_{-0.03}$
$\log F_{0.5-10\text{keV}}^{\text{bb}}$	$-12.80^{+0.06}_{-0.07}$	$-13.8^{+0.2}_{-0.7}$	$-13.4^{+0.2}_{-0.5}$	$-12.83^{+0.14}_{-0.24}$	$-13.40^{+0.13}_{-0.20}$	$-13.37^{+0.15}_{-0.23}$
powerlaw						
Γ	$2.78^{+0.09}_{-0.09}$	$2.80^{+0.04}_{-0.08}$	$2.2^{+0.4}_{-0.4}$	$2.37^{+0.18}_{-0.18}$	$1.7^{+0.8}_{-0.8}$	$2.48^{+0.19}_{-0.21}$
$\log F_{0.5-10\text{keV}}^{\text{pl}}$	$-12.44^{+0.03}_{-0.03}$	$-12.08^{+0.01}_{-0.01}$	$-12.96^{+0.09}_{-0.12}$	$-12.22^{+0.03}_{-0.03}$	$-13.30^{+0.19}_{-0.14}$	$-12.72^{+0.03}_{-0.04}$
relline						
E_{line} (keV)		6.7^*				
q_{in}		> 6				
q_{out}		3^*				
R_{br} (r_{ISCO})		$2.1^{+0.7}_{-0.3}$				
a_*		> 0.97				
Incl (deg)		64^{+11}_{-12}				
$\log F_{0.5-10\text{keV}}^{\text{relline}}$		$-13.0^{+0.3}_{-0.2}$				
$\chi^2/d.o.f.$	168.83/179	253.05/238	8.15/16	116.96/126	3.15/9	38.01/39

**Figure 4.** Γ versus $\log \lambda_{\text{Edd}}$. Red circles are our NLS1 sample using the k_{bol} measured by Equation 1; blue squares and grey up-pointing triangles are NLS1s and BLS1s at lower redshifts in GW+20; purple down-pointing triangles are our NLS1 sample using the k_{bol} in GW+20. The solid line represents the linear regression obtained for the clean NLS1s and BLS1s in GW+20.

spectra of our higher-redshift sample and the local sample in GW+20 have comparable energy ranges in the rest frame.

Figure 5 shows the soft excess strength versus the Eddington ratio. While the NLS1s in GW+20 show a variety of soft excess strengths, they present similar values of the Eddington ratio. This is also the case for the BLS1s in grey points. In particular, the NLS1s show relatively stronger soft excess strength than the BLS1s. Our NLS1s show a similar range of soft excess strength despite the relatively lower λ_{Edd} . Among them, WISEA J033429 presents the highest SX1 and SX2 and the second lowest SX3. SX3 is imprinted with the absolute strength of the soft excess, as it compares the soft X-ray luminosity directly with the Eddington luminosity and thus is susceptible to the Eddington ratio. SX1 and SX2 can be a better indicator of the strength of the soft excess relative to the powerlaw continuum, regardless of the bolometric luminosity of the source.

Figure 6 shows the photon index Γ versus the soft excess strength. GW+20 presented a positive $\Gamma - \text{SX}$ correlation in their AGN sam-

ple. Though our sources roughly follow a similar trend, we cannot be conclusive about a similar correlation due to the small number of sources. PG 1543+489 is the outlier in our sample. The soft excess strength is weak (lowest SX1, SX2, and SX3 in the sample), while it shows a very soft powerlaw continuum. It is also one of the most massive and luminous sources in our sample and the NLS1s in GW+20.

The high redshifts of our sample move a great portion of the soft excess emission beyond the lower limits of the detection range. The lack of observation above 10 keV in the observed frame also makes it hard to accurately identify the continuum. These factors would likely cause a degeneracy between the soft excess component and the powerlaw component, and thus a large uncertainty in SX1 and SX2. To better illustrate the degeneracy, we plot the constraints on the flux of the bbody component from 0.5 – 10 keV and the powerlaw photon index for SDSS J024651 in Figure 7. Although the confidence levels shown with the contours are consistent with the uncertainties in Table 3, the “banana-shaped” contours clearly show the degeneracy between the soft excess flux and the photon index. Within 99% confidence level, two possible solutions are found to explain the data with similarly good fits: (1) $\Gamma = 2.6$ and $\log F_{0.5-10\text{keV}}^{\text{bb}} = -13.2$ (2) $\Gamma = 2.0$ and $\log F_{0.5-10\text{keV}}^{\text{bb}} = -12.4$.

PG1543+489 is the only source in our sample that shows a blurred iron line feature. By modeling the emission line with the relativistic line emission model `relline`, we would be able to probe the innermost region of the accretion disk. The results indicate a fast-spinning BH ($a_* > 0.97$). The emissivity profile shows a steep powerlaw ($q_{\text{in}} > 6$) within a relatively small radius ($R_{\text{br}} = 2.1^{+0.7}_{-0.3}$). This scenario indicates a strong illumination from the primary source onto the innermost disk region, where the relativistic effect can play a significant role in the outgoing reflection spectrum. This is consistent with the blurred iron line feature observed in this source.

3.4 The $\alpha_{\text{OX}} - L_{2500 \text{ \AA}}$ relation

Apart from the X-ray observations, we also incorporate their historical observations at the optical and UV wavelengths. In particular, we focus on their rest-frame 2500 \AA monochromatic luminosities $L_{2500 \text{ \AA}}$ and optical-to-X-ray spectral indices α_{OX} .

The α_{OX} is defined as $\alpha_{\text{OX}} \equiv \log(f_{\text{X}}/f_{\text{UV}})/\log(\nu_{\text{X}}/\nu_{\text{UV}}) = 0.3838 \log(f_{\text{X}}/f_{\text{UV}})$, where f_{X} and f_{UV} are the 2 keV and 2500 \AA rest-frame flux density; ν_{X} and ν_{UV} are their corresponding frequen-

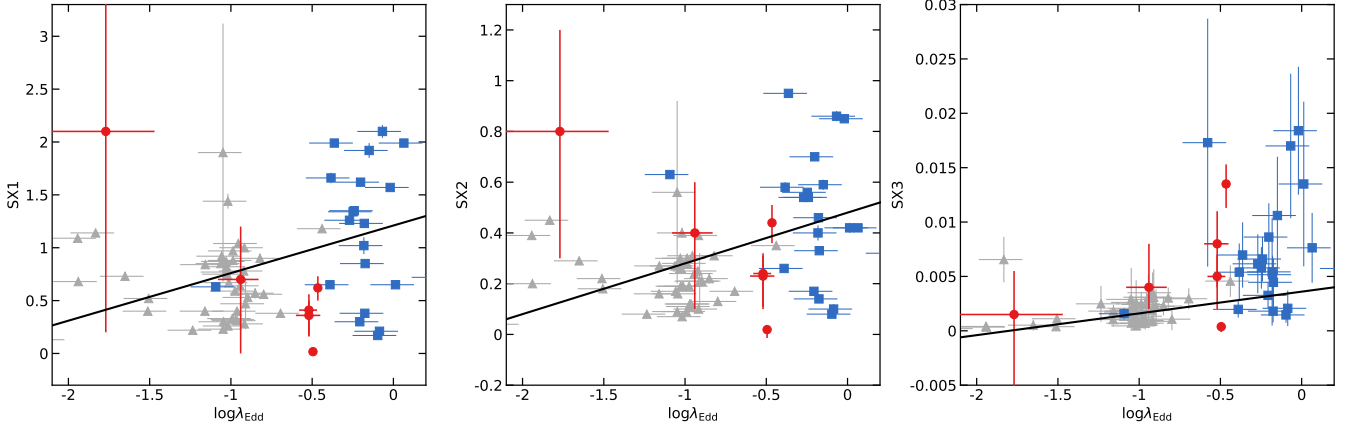


Figure 5. Soft excess strength versus $\log \lambda_{\text{Edd}}$. Red circles are our high-redshift NLS1 sample; blue squares and grey triangles are NLS1s and BLS1s in GW+20. The solid line represents the linear regression obtained for the clean NLS1s and BLS1s in GW+20.

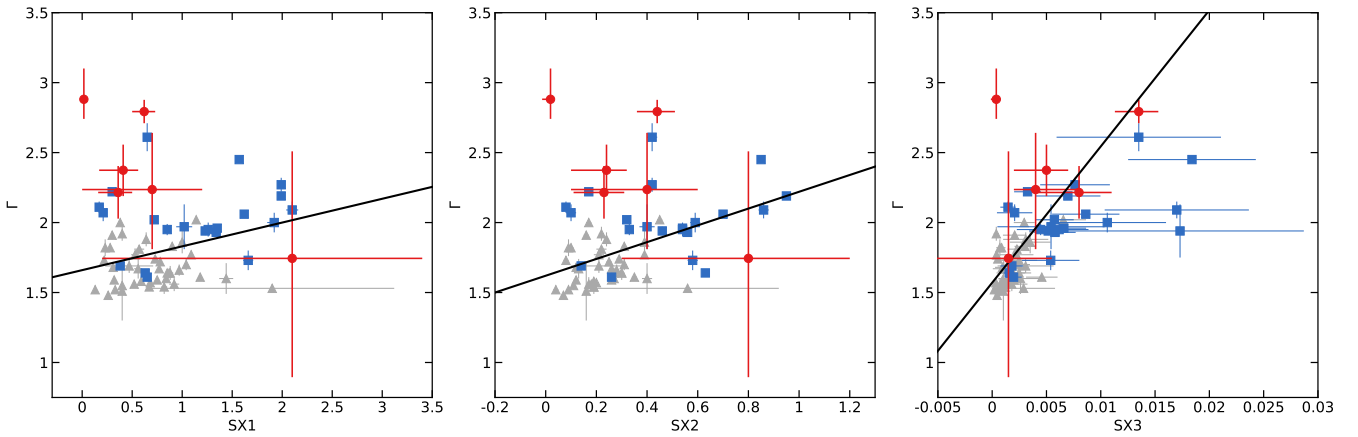


Figure 6. Γ versus $SX1$, $SX2$, and $SX3$. Red circles are our high-redshift NLS1 sample; blue squares and grey triangles are NLS1s and BLS1s in GW+20. The solid line represents the linear regression obtained for the clean NLS1s and BLS1s in GW+20.

cies. Previous studies have revealed a strong anti-correlation between α_{OX} and $L_{2500 \text{ \AA}}$ (e.g., [Strateva et al. 2005](#); [Just et al. 2007](#)). The “simple” NLS1s defined by [Gallo \(2006\)](#) follow the correlation relatively well and appear to be in a typical flux state, while the “complex” NLS1 sample is representative of objects in X-ray low-flux states. They can be greatly below the nominal $\alpha_{\text{OX}} - L_{2500 \text{ \AA}}$ relation and present stronger X-ray variability.

We search the archived f_{UV} values and measure the f_{X} according to the best-fitting baseline models of our sources. The host-galaxy contribution is not subtracted from the UV observations, introducing a level of uncertainty. The flux and the corresponding α_{OX} values are summarized in columns (4), (5), and (6) of Table 2. We plot the α_{OX} versus the $L_{2500 \text{ \AA}}$ in Figure 8. Most of our higher-redshift sources show good consistency with the $\alpha_{\text{OX}} - L_{2500 \text{ \AA}}$ relation of radio-quiet type 1 AGNs in [Strateva et al. \(2005\)](#) except for WISEA J033429. This object is significantly X-ray weak, with $\Delta\alpha_{\text{OX}} = \alpha_{\text{OX,obs}} - \alpha_{\text{OX,exp}} = -0.50$ from the relation, corresponding to an X-ray weakness $f_{\text{weak}} = 10^{-\Delta\alpha_{\text{OX}}/0.3838} = 20.1$. The X-ray weakness indicates the L_{bol} of WISEA J033429 estimated from the X-rays is underestimated, which is consistent with

the discrepancy between the X-ray and the optical Eddington ratios ($\log \lambda_{\text{Edd,X}} = -1.60$; $\log \lambda_{\text{Edd,opt}} = -0.55$) shown Table 2. However, as this source also shows the strongest soft excess emission relative to the continuum ($SX1$ and $SX2$), the X-weakness is likely to be intrinsic. The light-bending effect in the relativistic reflection model may have an important role. In this case, most of the primary emission from the primary source is bent back toward the BH, causing an X-ray low-flux state ([Ross & Fabian 2005](#)).

4 DISCUSSION

4.1 Systematic Uncertainties and Selection Effects

Here we discuss the systematic effects of our measurement using the baseline models. We note that the most prominent systematic effect lies in the estimation of k_{bol} . For a majority of the NLS1s in GW+20, k_{bol} were estimated as the average value obtained by the NLS1 sample in [Vasudevan & Fabian \(2009\)](#). The average bolometric correction factor for NLS1s in [Vasudevan & Fabian \(2009\)](#) is 96.4. If we apply Equation 1 to the NLS1s in GW+20, based on their rest-frame 2–10

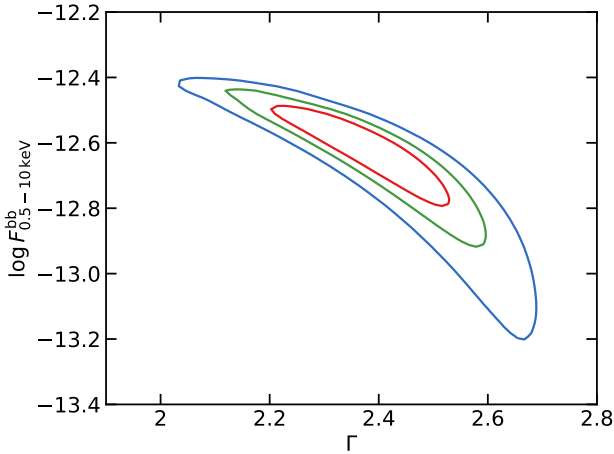


Figure 7. Constraints on the flux of the bbody component ($\log F_{0.5-10\text{keV}}^{\text{bb}}$) and the powerlaw photon index (Γ) for the source SDSS J024651. The red, green, and blue curves represent 68%, 90%, and 99% confidence levels for two relevant parameters, respectively. The banana-shaped contours clearly show a degeneracy between bbody and powerlaw component.

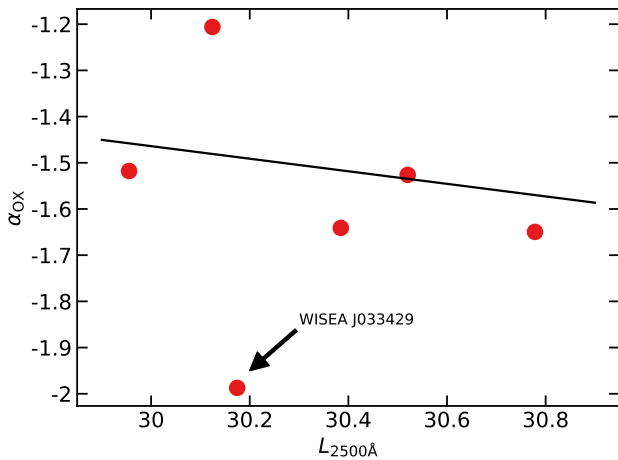


Figure 8. The α_{OX} versus the 2500 Å monochromatic luminosity $L_{2500\text{Å}}$. The red-filled circles are our NLS1s. The solid black line is the dependence of α_{OX} for radio-quiet type-1 AGNs ($\alpha_{\text{OX}} = -0.136L_{2500\text{Å}} + 2.616$) as in [Strateva et al. \(2005\)](#). The most X-ray weak source WISEA J033429 is marked in the plot.

keV luminosity, the estimated k_{bol} should be $\sim 15-30$. Thus, λ_{Edd} in GW+20 should be overestimated by a factor of $\sim 3-6$, corresponding to a difference of $0.5-0.8$ dex for $\log \lambda_{\text{Edd}}$. If we consider this effect in the estimation of λ_{Edd} , the separation between the two samples can naturally be resolved. We test this hypothesis by applying $k_{\text{bol}} = 96.4$ as in GW+20 to our NLS1s at higher redshift. We plot the results in purple in Figure 4. Our NLS1s at higher redshift now have similar λ_{Edd} and Γ with the GW+20 NLS1s at lower redshift. This suggests the estimation of k_{bol} can lead to large systematic uncertainties. We emphasize that it does not indicate the estimation of k_{bol} in [Netzer \(2019\)](#) is inconsistent with the one in [Vasudevan & Fabian \(2009\)](#). Rather, the discrepancy in λ_{Edd} is because a constant k_{bol} may only work for AGNs with a relatively low λ_{Edd} ([Vasudevan &](#)

[Fabian 2009](#)). As our sources show large λ_{Edd} (> 0.1), we prefer an increasing k_{bol} as the measured X-ray luminosities increase, as shown in Equation 1. GW+20 did not consider the dependence of k_{bol} on λ_{Edd} , and they did not exclude the outliers in the NLS1 samples of [Vasudevan & Fabian \(2009\)](#), which can lead to a highly overestimated average k_{bol} .

Another systematic effect results from the instrumental selection. Our sources have higher redshift, so they need higher absolute luminosity to be detected. On the other hand, they also show larger BH masses, which means they can be more luminous even with a similar λ_{Edd} . This is consistent with the results in Figure 4 after considering the systematic effect on k_{bol} .

A discrepancy in the methods between this work and GW+20 is that GW+20 applied the bulk-motion Comptonization model `bmc` to model the continuum ([Shrader & Titarchuk 1999](#)), rather than the `powerlaw` model we use here. The `bmc` model includes four parameters: the seed photon temperature kT_{seed} , the spectral index α , the Comptonization parameter A , and the normalization. We test the `bmc` model by fixing $kT_{\text{seed}} = 0.01$ keV and allow other parameters to vary. The `bmc` model provides almost the same best-fit results, and the difference of Γ compared with our baseline models is less than 0.02, much smaller than the discrepancy detected in Figure 4. We thus consider the discrepancy in the baseline models to be negligible.

So far we find that all our sources have significant soft excess despite that they have slightly lower or similar λ_{Edd} at higher redshift. We also apply a phenomenological model to quantify the soft excess. Now we want to use more physical models to discuss the origin of the soft excess.

4.2 The Warm Corona Model

In this section, we discuss the possibility of the warm corona model as the origin of the soft excess emission of our sources ([Magdziarz et al. 1998](#); [Petrucci et al. 2018](#)). Under this hypothesis, the seed UV photons are up-scattered by a warm and optically thick corona. The soft excess is the high-energy tail of the Comptonized component. To do so, we replace the bbody component in our baseline models with the `nthcomp` model ([Życki et al. 1999](#)) to provide a more physical description of the soft excess. The `nthcomp` model describes the thermally Comptonized continuum produced in the warm corona. The model considers disk multi-temperature black-body emission with seed photon temperature at kT_{bb} as the seed spectrum. We fix $kT_{\text{bb}} = 10$ eV as we only analyze the spectra in the X-ray band. The produced continuum can be easily controlled by the warm corona temperature $kT_{\text{e,w}}$ and the asymptotic powerlaw photon index Γ_{w} . The powerlaw continuum is also replaced by the `cutoffpl` model with the high-energy cutoff fixed at 300 keV (we replace the `powerlaw` model with the `cutoffpl` model because we want to have a consistent model setup with Section 4.3; see the description therein). As N_{H} is unconstrained in our baseline models, we fix the N_{H} to Galactic values. The full model in Xspec is

`const×TBabs×zshifft×(nthcomp+cutoffpl)`.

For PG 1543+489, we still add a `relline` component to model the iron $K\alpha$ line feature. We assume a broken-powerlaw emissivity profile with variable q_{in} and R_{br} with $\epsilon(r) \propto \epsilon^{-3}$ at $r > R_{\text{br}}$, which is the same as the treatment in the baseline model. We fix the line energy in the rest frame at $E_{\text{line}} = 6.7$ keV. Other free parameters in the `relline` model are the spin (a_*), and the inclination angle. The inner radius of the disk is assumed to reach the innermost stable circular orbit (r_{ISCO}).

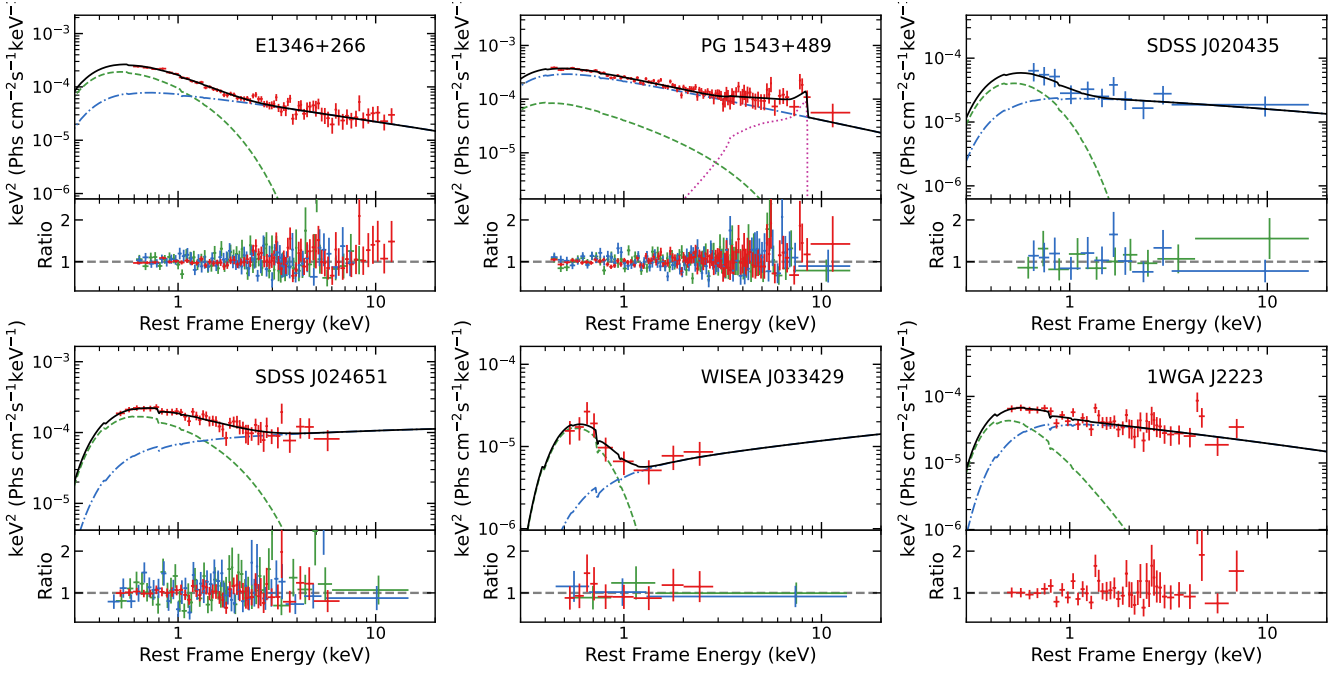


Figure 9. Warm corona model fits. Unfolded best-fit model plots and data-to-model ratio plots for each NLS1. The upper plots show the best-fit models. We only show pn data in red for clarity (MOS1 data in blue for SDSS J020435). Solid black lines: the total model; blue dash-dotted lines: `cutoffpl`; green dashed lines: `nthcomp`; purple dotted lines: `relline`. The lower plots show the data-to-model ratios. The red, blue, and green data points correspond to pn, MOS1, and MOS2 data.

Table 4. Best-fit table of the warm corona models. The flux F is in units $\text{erg s}^{-1} \text{cm}^{-2}$. The reported uncertainties correspond to the 90% confidence level for one parameter ($\Delta\chi^2 = 2.71$). * indicates that the parameter is frozen in the fit. Δ means the parameter cannot be constrained.

	E1346+266	PG1543+489	SDSS J0204	SDSS J0246	WISEA J033	1WGA J2223
nthcomp						
Γ_w	$3.0^{+0.6}_{-1.3}$	$3.1^{+0.8}_{-0.4}$	< 7	$2.9^{+0.4}_{-1.2}$	$2.1 \pm \Delta$	$5.0^{+0.6}_{-0.4}$
$kT_{e,w}$ (keV)	> 0.17	$0.83 \pm \Delta$	> 1.1	> 0.16	< 1	> 0.06
$\log F_{0.3-10\text{keV}}^{\text{nth}}$	$-11.9^{+0.2}_{-0.3}$	$-12.5^{+0.6}_{-0.9}$	$-12.7^{+0.5}_{-0.5}$	$-12.0^{+0.2}_{-0.4}$	$-12.8^{+0.5}_{-0.3}$	$-12.3^{+0.5}_{-0.6}$
cutoffpl						
Γ_h	$2.5^{+0.2}_{-1.3}$	$2.7^{+0.7}_{-0.4}$	$2.2^{+0.4}_{-2.0}$	$1.9^{+0.5}_{-0.8}$	$1.7^{+0.8}_{-1.0}$	$2.4^{+0.3}_{-0.4}$
$\log F_{0.3-10\text{keV}}^{\text{pl}}$	$-12.1^{+0.2}_{-0.9}$	< -11.7	$-12.7^{+0.1}_{-0.4}$	$-12.1^{+0.2}_{-0.4}$	$-13.3^{+0.2}_{-0.1}$	$-12.5^{+0.1}_{-0.2}$
relline						
E_{line} (keV)		6.7^*				
q_{in}		> 7				
q_{out}		3^*				
R_{br} (r_{ISCO})		$1.7^{+0.8}_{-0.2}$				
a_*		> 0.97				
Incl (deg)		61^{+14}_{-9}				
$\log F_{0.3-10\text{keV}}^{\text{relline}}$		$-13.0^{+0.2}_{-0.3}$				
$\chi^2/d.o.f.$	164.82/178	252.69/237	8.22/15	113.83/125	3.29/8	37.73/38

Figure 9 shows the best-fit models and data/model ratio plots for the warm corona scenario. The best-fit results are summarized in Table 4. The `relline` component indicates a fast-spinning BH and a steep powerlaw emissivity profile, consistent with the results where the `bbbody` model is used for the soft excess.

Our sources present a highly scattered X-ray continuum ($\Gamma_h = 1.7-2.7$) and a warm corona emission with very low temperature and large photon index ($kT_{e,w} < 0.9 \text{ keV}$, $\Gamma_w > 2.1$). This is consistent with the sample study in Petrucci et al. (2018) where 100 observations of 22 objects were studied (see Figure 5 therein).

We visualize the warm corona photon index Γ_w and the warm

corona temperature $kT_{e,w}$ in Figure 10, and the contours of optical depth τ are also plotted according to Equation (13) in Beloborodov (1999). Open circles mean either the temperature or the optical depth of the warm corona is unconstrained. We see that all sources show large $\tau > 5$ except for SDSS J020435, which has an upper limit of Γ_h and a lower limit of $kT_{e,w}$. This is in agreement with the previous studies of the warm corona in AGNs (e.g. Jin et al. 2012; Petrucci et al. 2013, 2018).

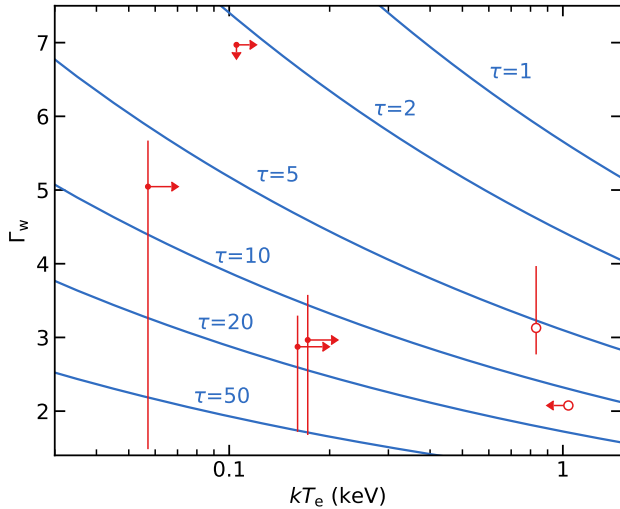


Figure 10. Best-fit warm corona photon index Γ_w versus temperature kT_e (red points). The solid blue curves are the contours of the optical depth τ based on Equation (13) in Beloborodov (1999). Open circles mean either the temperature or the optical depth of the warm corona is unconstrained.

4.3 The Relativistic Disk Reflection Model

Another model commonly applied to explain the soft excess is the relativistic reflection model (Crummy et al. 2006; Fabian et al. 2009; Jiang et al. 2018b). The X-ray fluorescence emission is produced by the reprocessing of photons by the inner part of the disk. These fluorescence features will be blurred by the strong relativistic effects around the BH. This effect makes X-ray reflection spectroscopy one of the most effective tools in probing the vicinity of BH. Moreover, the existence of high-density inner-disk electrons ($n_e > 10^{15} \text{ cm}^{-3}$) would further contribute to an increased emission in the soft X-ray band (Ross & Fabian 1993; Garca et al. 2016).

Currently, the most advanced reflection model package is `relxill` (Dauser et al. 2013; Garca et al. 2014). It incorporates `xillver`, which calculates the reflection in the rest-frame of the accretion disk, and the relativistic convolution model `relconv`. Specifically, to model the reflection component we apply the `relxillD` flavor which considers a variable disk electron density ($10^{15} < n_e < 10^{19} \text{ cm}^{-3}$) and a fixed high-energy cutoff at 300 keV. The primary effect of the high density is the increase of free-free heating in the deeper region of the disk, causing an increased disk temperature. The emission of the reflected spectrum at low energies would thus increase and may consequently resolve the existence of the soft excess (Garca et al. 2016; Jiang et al. 2019). The continuum is described by `cutoffpl`. The high-energy cutoff is also fixed at 300 keV to keep a consistent setup with the `relxillD` model (although the exact cutoff value is not important with our data up to 10 keV in the observed frame). We fix the N_H to Galactic values as we did in the previous analysis. The full model in Xspec notation is

`const*TBabs*zashift*(cutoffpl+relxillD)`.

Since the hard continuum is treated as the incident spectrum of the reflection component, we link the photon index of `relxillD` with the spectral slope Γ_h of `cutoffpl`. For all observations, we assume a powerlaw-like disk emissivity profile $\epsilon(r) \propto r^{-q}$. The inner radius of the disk is assumed to reach the ISCO. In a nominal fit, we allow a variable spin (a_*), inclination angle, disk ionization (ξ), iron

abundance (A_{Fe}), and disk density (n_e). If neither the upper nor lower limit of n_e can be constrained, we fix $n_e = 10^{15} \text{ cm}^{-3}$, as in the case of the standard `relxill` flavor. If the spin cannot be constrained, we fix $a_* = 0.998$. We also check that allowing a free inner disk radius R_{in} would only result in a $\Delta\chi^2 \approx -0.4$ compared with a fixed $R_{in} = R_{ISCO}$. Thus, we choose to fix the R_{in} at the ISCO. If there are other unconstrained parameters, we would further decrease the degrees of freedom by fixing $q = 3$, $\theta = 45^\circ$, and $A_{Fe} = 1$. In the end, for the least constrained fit, the only free parameters are the photon index Γ_h and the ionization parameter ξ , in addition to the normalization.

Figure 11 shows the best-fit models and data/model ratio plots for the relativistic reflection model. Table 5 summarizes the best-fit parameter values. The relativistic reflection model provides similarly good fits compared with the warm corona model. All sources show a very soft continuum with $\Gamma_h > 2.2$ except for WISEA J033429. This source shows the most significant X-ray weakness, and it has a large uncertainty on Γ_h with an upper limit value of 2.4 within 90% confidence level. The co-existence of the X-ray weakness and the strong SX1 and SX2 in this source can be explained by the relativistic reflection. The relativistic reflection blurs a series of emission lines in the soft X-ray band, causing an “excess” of emission; in the meantime, the light-bending effect causes a portion of the primary emission from the hot corona to bend towards the BH and thus results in an X-ray low-flux state. Our spectral fitting confirms a reflection-dominated spectrum in WISEA J033429 (Figure 11), which further supports the relativistic reflection. The conclusion is similar to the one in Garca et al. (2019), in which they studied a nearby ($z = 0.0344$) bright Seyfert 1 AGN Mrk 509.

Interestingly, our sources show slightly higher ionization than typical Sy1s ($\log \xi = 1 - 2$, see e.g., Walton et al. 2013). A high ionization can contribute to the soft excess together with a high-density disk. The BH spins of these sources are also not well constrained due to a low SNR in the iron band. The most stringent constraints come from E1346+266 and PG 1543+489. Both sources indicate a rapidly spinning BH ($a_* > 0.94$ and $a_* > 0.81$, respectively).

According to the standard α -disk model by Shakura & Sunyaev (1973), Svensson & Zdziarski (1994) gave a relationship between the density of a radiation-pressure-dominated disk at radius r and the accretion rate

$$n_e(r) = \frac{1}{\sigma_T R_S} \frac{256\sqrt{2}}{27} \alpha^{-1} r^{3/2} \dot{m}^{-2} \left[1 - (R_{in}/r)^{1/2} \right]^{-2} [\xi'(1-f)]^{-3}, \quad (2)$$

where σ_T is the Thompson cross section, $R_S \equiv 2GM_{BH}/c^2$ is the Schwarzschild radius, and r is the radius on the disk in units of R_S . We take $\alpha = 0.1$ as the standard viscosity parameter (Shakura & Sunyaev 1973), and $\xi' = 1$ in the radiative diffusion equation, and f is the fraction of the total transported accretion power released from the disk to the hot corona (Xu et al. 2021). The dimensionless accretion rate \dot{m} is defined as $\dot{m} \equiv \dot{M}/\dot{M}_{crit} = L/\eta L_{Edd}$, where η is the efficiency for converting accreted mass into outgoing radiation. $\eta = 0.057$ for a Schwarzschild BH ($a_* = 0$) and $\eta = 0.32$ for a maximally spinning Kerr BH ($a_* = 0.998$) (Thorne 1974). We assume $\eta = 0.19 \pm 0.13$ in our analysis so that it takes into account all possible values of η , and we propagate the uncertainties to the estimated accretion rates of our sample. According to Equation 2, $\log n_e \propto -\log(M_{BH}\dot{m}^2)$.

Figure 12 shows $\log n_e$ versus $\log(M_{BH}\dot{m}^2)$. The solid lines show the analytic solution for different values of f assuming $r = 2R_S$. The red points are the high- z sources in our sample, and the grey points are the samples studied in Jiang et al. (2019). The open circles

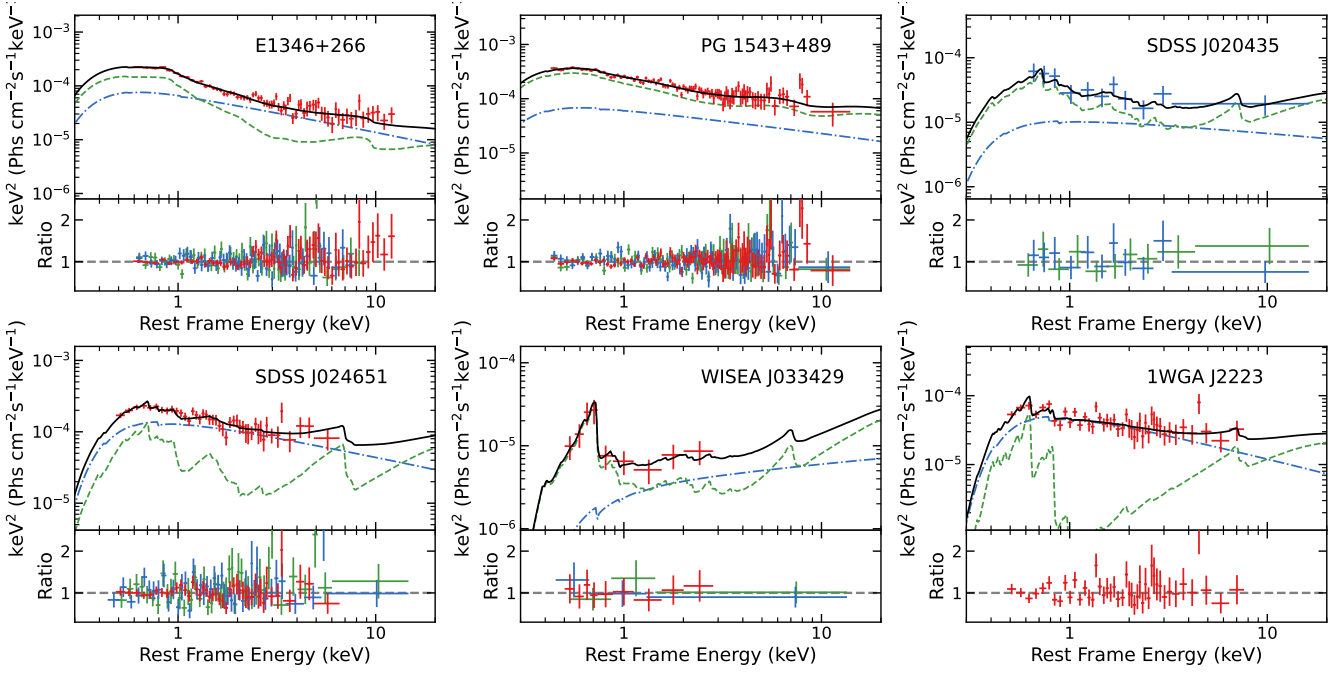


Figure 11. Relativistic reflection model fits. Unfolded best-fit model plots and data-to-model ratio plots for each high-redshift NLS1. The upper plots show the best-fit models. We only show pn data in red for clarity (MOS1 data in blue for SDSS J020435). Solid black lines: the total model; blue dash-dotted lines: cutoffpl; green dashed lines: relxillD. The lower plots show the data-to-model ratios. The red, blue, and green data points correspond to pn, MOS1, and MOS2 data.

Table 5. Best-fit table of relativistic reflection models. The ionization parameter ξ is in unit erg cm s^{-1} . The disk electron density n_e is in units cm^{-3} . The flux F is in units $\text{erg s}^{-1} \text{cm}^{-2}$. The reported uncertainties correspond to the 90% confidence level for one parameter ($\Delta\chi^2 = 2.71$). * indicates that the parameter is frozen in the fit.

	E1346+266	PG1543+489	SDSS J0204	SDSS J0246	WISEA J033	1WGA J2223
cutoffpl						
Γ_h	$2.70^{+0.10}_{-0.12}$	$2.44^{+0.06}_{-0.07}$	$2.2^{+0.8}_{-0.3}$	$2.5^{+0.1}_{-0.3}$	$1.7^{+0.7}_{-0.3}$	$2.69^{+0.16}_{-0.17}$
$\log F_{0.3-10\text{keV}}^{\text{pl}}$	$-12.2^{+0.2}_{-0.2}$	< -12.0	< -12.5	$-12.0^{+0.1}_{-0.8}$	< -13.2	$-12.39^{+0.04}_{-0.06}$
relxillD						
q	> 6.2	> 3	3^*	> 0.2	3^*	3^*
a_*	> 0.95	> 0.81	0.998^*	0.998^*	0.998^*	0.998^*
Incl (deg)	82^{+4}_{-16}	69^{+4}_{-57}	45^*	39^{+24}_{-25}	45^*	45^*
$\log \xi$	$3.0^{+0.4}_{-0.2}$	$3.3^{+0.4}_{-1.4}$	< 3.5	$2.0^{+1.1}_{-0.6}$	$2.3^{+0.9}_{-0.7}$	< 1.4
$A_{\text{Fe}} (A_{\text{Fe},\odot})$	> 1.1	$0.9^{+1.3}_{-0.2}$	1^*	> 3.2	1^*	1^*
$\log n_e$	$17.4^{+1.1}_{-0.9}$	< 18	15^*	< 18	> 17.9	15^*
$\log F_{0.3-10\text{keV}}^{\text{relxill}}$	$-11.99^{+0.19}_{-0.19}$	$-11.8^{+0.2}_{-0.4}$	$-12.6^{+0.2}_{-0.8}$	$-12.3^{+0.4}_{-0.3}$	$-13.0^{+0.4}_{-0.3}$	$-12.9^{+0.1}_{-0.2}$
$\chi^2/d.o.f.$	163.83/174	254.95/239	8.37/16	107.09/121	2.71/8	37.61/39

indicate that the results cannot be constrained. Taking into account the uncertainties in $\log n_e$, our sources roughly follow the trend as predicted in Svensson & Zdziarski (1994) that a system with lower $\log M_{\text{BH}}$ tends to have higher n_e . The only source with constrained measurements of n_e is E1346+266, which has the largest mass and highest redshift among our sources. In this source, about 95% of the energy in the disk is released to the corona, and the radiation-pressure dominated region is $r < 2R_s$ to explain the inferred high disk density.

5 CONCLUSION

We performed a detailed spectral analysis of six NLS1s at $z = 0.35 - 0.92$ using XMM-Newton EPIC data. Our samples show large BH

masses at the upper end of the local samples ($\log M_{\text{BH}} > 7.5$) and slightly lower or similar λ_{Edd} . We discover that all these sources have strong soft excess emission below 2 keV with relatively soft continuum.

After confirming the existence of the soft excess emission, we use the phenomenological bbody model to quantify the soft excess strength and compare the results from our higher-redshift sample with the local NLS1s and BLS1s in GW+20. We find that the soft excess strength does not show much deviation from the previous sample. We also obtain the $\alpha_{\text{OX}} - L_{2500\text{\AA}}$ relation and find the most X-ray-weak source WISEA J033429 is intrinsically X-ray weak judging from its strong SX1 and SX2. We discuss in detail the impact of the bolometric correction factor k_{bol} , and conclude it carries the major systematic uncertainties in our measurements. The systematic

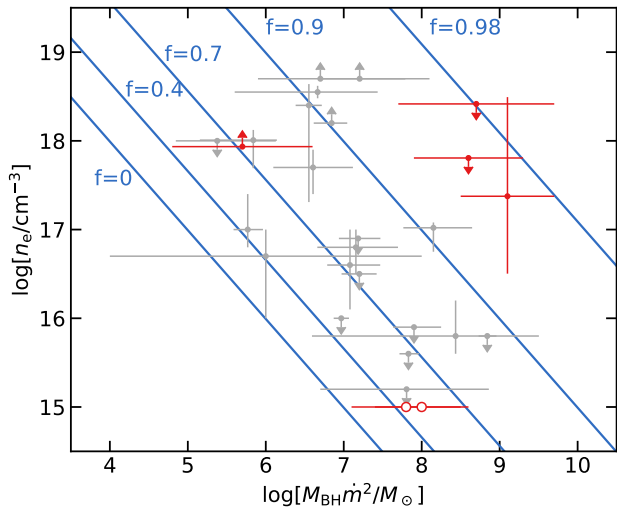


Figure 12. Disk electron density $\log n_e$ versus $\log(M_{\text{BH}}\dot{m}^2/M_{\odot})$. The grey points are the AGN samples considered in Jiang et al. (2019), and the red points are the high- z NLS1s in our sample. The solid blue lines are the solutions of disk density in Equation (8) in Svensson & Zdziarski (1994) at $r = 2R_s$ for $f = 0$ and $f = 0.9$, assuming $R_{\text{in}} = R_{\text{ISCO}} = 1.24R_g$ with $\xi' = 1$, $\alpha = 0.1$, $\eta = 0.19 \pm 0.13$ for a maximally spinning Kerr black hole. The open circles indicate that the results cannot be constrained.

difference of the estimated k_{bol} can explain the discrepancy of λ_{Edd} between our high-redshift sample and GW+20 sample. This further suggests the higher absolute luminosities of our sources are driven by BH mass rather than λ_{Edd} . For such detailed spectral analysis in our work, the high-redshift and the soft nature of the sources pose a great challenge for us to accurately identify the continuum, which results in a degeneracy in the parameters.

We then further consider more physical scenarios, the warm-corona model and the relativistic reflection model, to account for the soft excess. These two models provide almost equally good fits. They also allow us to probe the properties of the innermost region of the AGNs. We show that in the warm-corona scenario, the warm coronae of our sample have a low temperature ($kT_{e,w} \approx 0.1 - 1$ keV) and large optical depth ($\tau = 5 - 20$); in the reflection scenario, the sources show relatively higher ionization than the samples in Walton et al. (2013). We are also able to constrain the high spin values of several sources. Combining both facts that WISEA J033429 shows the strongest relative soft excess strength with respect to the continuum emission and it shows a reflection-dominated spectrum, we tentatively conclude the relativistic reflection is a more promising explanation for the soft excess, though we cannot exclude the warm corona model based on the statistics in the entire. Detailed tests of different models for the soft excess are better carried out with bright local samples, which is beyond the scope of this work.

The low SNR in the iron line band does not allow us to identify the iron line feature confidently. Observations from future X-ray missions like *Athena* may be able to provide better constraints on the spectral shape. The large effective area and energy resolution in the iron line band would allow us to better model the reflection spectrum and might help determine the contribution to the soft excess (Parker et al. 2022).

While both the warm-corona and relativistic reflection are possible explanations for the soft excess, it is natural to consider reflection from the disk in addition to Comptonization in a warm corona (Xu

et al. 2021). Recently, Xiang et al. (2022) used a new model *reXcor* that self-consistently combines a warm corona and ionized reflection, and analyzes two Seyfert galaxies HE 1131-1820 and NGC 4593. Although the geometry of the systems is much simplified, the model was able to produce several broadened reflection features with a variety of shapes of the soft excess. Such a type of model may provide new insights about the NLS1s at higher redshift.

ACKNOWLEDGEMENTS

Z.Y. thanks Mario Gliozzi for sharing the data in GW+20 and acknowledges support from the Verne M. Willaman Distinguished Graduate Fellowships in Science. J.J. acknowledges support from the Leverhulme Trust, the Isaac Newton Trust, and St Edmund's College.

DATA AVAILABILITY

The data underlying this article are available in the High Energy Astrophysics Science Archive Research Center (HEASARC), at <https://heasarc.gsfc.nasa.gov>. The *relxill* package can be downloaded at <http://www.sternwarte.uni-erlangen.de/~dauser/research/relxill/>.

REFERENCES

- Alston W. N., et al., 2020, *Nature Astronomy*, 4, 597
- Arnaud K. A., 1996, in Jacoby G. H., Barnes J., eds, *Astronomical Society of the Pacific Conference Series Vol. 101, Astronomical Data Analysis Software and Systems V*. p. 17
- Bambi C., et al., 2021, *Space Sci. Rev.*, 217, 65
- Baskin A., Laor A., 2004, *MNRAS*, 350, L31
- Beloborodov A. M., 1999, in Poutanen J., Svensson R., eds, *Astronomical Society of the Pacific Conference Series Vol. 161, High Energy Processes in Accreting Black Holes*. p. 295 ([arXiv:astro-ph/9901108](https://arxiv.org/abs/astro-ph/9901108))
- Bianchi S., Guainazzi M., Matt G., Fonseca Bonilla N., Ponti G., 2009, *A&A*, 495, 421
- Boissay R., Ricci C., Paltani S., 2016, *A&A*, 588, A70
- Boller T., Brandt W. N., Fink H., 1996, *A&A*, 305, 53
- Boroson T. A., 2002, *ApJ*, 565, 78
- Boroson T. A., Green R. F., 1992, *ApJS*, 80, 109
- Crummey J., Fabian A. C., Gallo L., Ross R. R., 2006, *MNRAS*, 365, 1067
- Dauser T., Wilms J., Reynolds C. S., Brenneman L. W., 2010, *MNRAS*, 409, 1534
- Dauser T., Garcia J., Wilms J., Böck M., Brenneman L. W., Falanga M., Fukumura K., Reynolds C. S., 2013, *MNRAS*, 430, 1694
- Fabian A. C., Rees M. J., Stella L., White N. E., 1989, *MNRAS*, 238, 729
- Fabian A. C., Ballantyne D. R., Merloni A., Vaughan S., Iwasawa K., Boller T., 2002, *MNRAS*, 331, L35
- Fabian A. C., et al., 2009, *Nature*, 459, 540
- Fabian A. C., Lohfink A., Kara E., Parker M. L., Vasudevan R., Reynolds C. S., 2015, *MNRAS*, 451, 4375
- Frank J., King A., Raine D. J., 2002, *Accretion Power in Astrophysics: Third Edition*
- Gallo L. C., 2006, *MNRAS*, 368, 479
- Gallo L., 2018, in *Revisiting Narrow-Line Seyfert 1 Galaxies and their Place in the Universe*. p. 34 ([arXiv:1807.09838](https://arxiv.org/abs/1807.09838))
- García J., et al., 2014, *ApJ*, 782, 76
- García J. A., Fabian A. C., Kallman T. R., Dauser T., Parker M. L., McClintock J. E., Steiner J. F., Wilms J., 2016, *MNRAS*, 462, 751
- García J. A., et al., 2019, *ApJ*, 871, 88
- Gliozzi M., Williams J. K., 2020, *MNRAS*, 491, 532
- Goodrich R. W., 1989, *ApJ*, 342, 224

Grandi P., Foschini L., Masetti N., Palazzi E., 2004, *A&A*, **418**, 907

Grupe D., 2004, *AJ*, **127**, 1799

Grupe D., Mathur S., 2004, *ApJ*, **606**, L41

Grupe D., Beuermann K., Mannheim K., Thomas H. C., 1999, *A&A*, **350**, 805

Grupe D., Thomas H. C., Beuermann K., 2001, *A&A*, **367**, 470

Haardt F., Maraschi L., 1991, *ApJ*, **380**, L51

Jansen F., et al., 2001, *A&A*, **365**, L1

Jiang J., et al., 2018a, *MNRAS*, **477**, 3711

Jiang J., et al., 2018b, *MNRAS*, **477**, 3711

Jiang J., et al., 2019, *MNRAS*, **489**, 3436

Jiang J., Gallo L. C., Fabian A. C., Parker M. L., Reynolds C. S., 2020, *MNRAS*, **498**, 3888

Jin C., Done C., Ward M., Gierliński M., Mullaney J., 2009, *MNRAS*, **398**, L16

Jin C., Ward M., Done C., Gelbord J., 2012, *MNRAS*, **420**, 1825

Just D. W., Brandt W. N., Shemmer O., Steffen A. T., Schneider D. P., Chartas G., Garmire G. P., 2007, *ApJ*, **665**, 1004

Karttunen H., Kröger P., Oja H., Poutanen M., Donner K. J., 2007, *Fundamental astronomy*. Springer

Kaspi S., Smith P. S., Netzer H., Maoz D., Jannuzi B. T., Giveon U., 2000, *ApJ*, **533**, 631

Kelly B. C., Bechtold J., Trump J. R., Vestergaard M., Siemiginowska A., 2008, *ApJS*, **176**, 355

Laor A., 2019, *Nature Astronomy*, **3**, 374

Leighly K. M., 1999, *ApJS*, **125**, 297

Magdziarz P., Blaes O. M., Zdziarski A. A., Johnson W. N., Smith D. A., 1998, *MNRAS*, **301**, 179

Marinucci A., et al., 2014, *ApJ*, **787**, 83

Markoff S., Nowak M. A., Wilms J., 2005, *ApJ*, **635**, 1203

Middleton M., Done C., Gierliński M., 2007a, *MNRAS*, **381**, 1426

Middleton M., Done C., Gierliński M., 2007b, *MNRAS*, **381**, 1426

Miller J. M., 2007, *ARA&A*, **45**, 441

Miller J. M., et al., 2002, *ApJ*, **570**, L69

Miniutti G., Fabian A. C., 2004, *MNRAS*, **349**, 1435

Netzer H., 2019, *MNRAS*, **488**, 5185

Osterbrock D. E., Dahari O., 1983, *ApJ*, **273**, 478

Osterbrock D. E., Pogge R. W., 1985, *ApJ*, **297**, 166

Parker M. L., et al., 2014, *MNRAS*, **443**, 1723

Parker M. L., Miller J. M., Fabian A. C., 2018, *MNRAS*, **474**, 1538

Parker M. L., Matzeu G. A., Matthews J. H., Middleton M. J., Dauser T., Jiang J., Joyce A. M., 2022, *MNRAS*, **513**, 551

Peterson B. M., 1997, *An introduction to active galactic nuclei*. Cambridge University Press

Petrucchi P. O., et al., 2013, *A&A*, **549**, A73

Petrucchi P. O., Ursini F., De Rosa A., Bianchi S., Cappi M., Matt G., Dadina M., Malzac J., 2018, *A&A*, **611**, A59

Piconcelli E., Jimenez-Bailón E., Guainazzi M., Schartel N., Rodríguez-Pascual P. M., Santos-Lleó M., 2005, *A&A*, **432**, 15

Rakshit S., Stalin C. S., 2017, *ApJ*, **842**, 96

Rakshit S., Stalin C. S., Chand H., Zhang X.-G., 2017, *ApJS*, **229**, 39

Reynolds C. S., 2021, *ARA&A*, **59**, 117

Reynolds C. S., Nowak M. A., 2003, *Phys. Rep.*, **377**, 389

Ross R. R., Fabian A. C., 1993, *MNRAS*, **261**, 74

Ross R. R., Fabian A. C., 2005, *MNRAS*, **358**, 211

Shakura N. I., Sunyaev R. A., 1973, *A&A*, **24**, 337

Shen Y., et al., 2011, *ApJS*, **194**, 45

Shrader C. R., Titarchuk L., 1999, *ApJ*, **521**, L121

Sisk-Reynés J., Reynolds C. S., Matthews J. H., Smith R. N., 2022, *MNRAS*, **514**, 2568

Strateva I. V., Brandt W. N., Schneider D. P., Vanden Berk D. G., Vignali C., 2005, *AJ*, **130**, 387

Strüder L., et al., 2001, *A&A*, **365**, L18

Svensson R., Zdziarski A. A., 1994, *ApJ*, **436**, 599

Tanaka Y., Boller T., Gallo L., Keil R., Ueda Y., 2004, *PASJ*, **56**, L9

Thorne K. S., 1974, *ApJ*, **191**, 507

Turner M. J. L., et al., 2001, *A&A*, **365**, L27

Vasudevan R. V., Fabian A. C., 2009, *MNRAS*, **392**, 1124

Table A1. Candidate NLS1s for our analysis. The selected NLS1s are marked in boldface.

Full Name	<i>z</i>	XMM-Newton ObsID	EPIC-pn count rate upper limit (cts/s)
E1346+266	0.92	0109070201	0.310
PG 1543+489	0.40	0153220401	
		0505050201	0.512 (stacked)
		0505050701	
SDSS J014123.32+000752.8	0.97	0747430101	0.019
SDSS J020435.18–093154.9	0.62	0763910301	0.061
SDSS J024651.91–005930.9	0.47	0402320101	0.369
SDSS J150728.65+523137.6	0.85	0804620201	0.005
WISEA J033429.44+000610.9	0.35	0402320201	0.021
1WGA J2223.7–0206	0.46	0090050601	0.097

Vignali C., Piconcelli E., Bianchi S., Miniutti G., 2008, *MNRAS*, **388**, 761

Waddell S. G. H., Gallo L. C., 2020, *MNRAS*, **498**, 5207

Walton D. J., Nardini E., Fabian A. C., Gallo L. C., Reis R. C., 2013, *MNRAS*, **428**, 2901

Wang J.-G., et al., 2009, *ApJ*, **707**, 1334

Wilkins D. R., Fabian A. C., 2012, *MNRAS*, **424**, 1284

Willingale R., Starling R. L. C., Beardmore A. P., Tanvir N. R., O'Brien P. T., 2013, *MNRAS*, **431**, 394

Xiang X., et al., 2022, arXiv e-prints, p. arXiv:2206.06825

Xu Y., García J. A., Walton D. J., Connors R. M. T., Madsen K., Harrison F. A., 2021, *ApJ*, **913**, 13

Yuan W., et al., 2007, in Ho L. C., Wang J. W., eds, *Astronomical Society of the Pacific Conference Series Vol. 373, The Central Engine of Active Galactic Nuclei*. p. 529 (arXiv:astro-ph/0612470)

Życki P. T., Done C., Smith D. A., 1999, *MNRAS*, **309**, 561

APPENDIX A: CANDIDATE NLS1 SAMPLE

Here we present a list of candidate sources we have examined before our analysis in Table A1. These sources are identified as NLS1s in the optical bands. We examine their X-ray visibility in the XMM-Newton archive. We include the six sources with the highest count rates (> 0.020 cts/s) in our analysis.

This paper has been typeset from a \LaTeX file prepared by the author.